Melia *et al. Geothermal Energy* (2022) 10:11
https://doi.org/10.1186/s40517-022-00218-2

Geothermal Energy

RESEARCH Open Access

Physical property characterization of the Waipapa greywacke: an important geothermal reservoir basement rock in New Zealand

Aurelio Melia*, Daniel Roy Faulkner and David Daniel McNamara

*Correspondence:
aurelio.melia.geol@gmail.com

Department of Earth, Ocean and Ecological Sciences, University of Liverpool, Liverpool L69 3GP, UK

Abstract

Greywacke basement rocks in New Zealand host conventional geothermal reservoirs and may supply important hotter and deeper geothermal energy resources in the future. This work combines petrological analyses and physical property measurements of Waipapa greywacke, a basement unit hosting New Zealand geothermal reservoirs, in order to understand better how structurally controlled flow networks develop and channel geothermal fluids within it. Results show intact Waipapa greywacke has high tensile and triaxial compressive strengths, and low intrinsic permeability (~ 10^{-21} m^2). Permeability of intact Waipapa greywacke does not increase significantly during triaxial loading to failure and is accompanied by minimal changes ultrasonic wave velocities. These data taken together suggest that microcrack development during brittle deformation is very limited. Upon failure, the permeability increases by two orders of magnitude and shows similar permeability to tests performed on synthetic, single, mode I fractures in intact Waipapa greywacke. Permeability persists in Waipapa greywacke fractures under confining pressures of at least 150 MPa. It is concluded that Waipapa greywacke rocks will not allow fluid flow through the matrix of the rock and that substantial geothermal fluid flow will only occur through macrofracture networks.

Keywords: Geothermal, Greywacke, Permeability, Fracture, Rock properties, Basement rock

Introduction

In New Zealand, both direct use (e.g. heating, bathing, horticulture) and electricity production from geothermal resources is well developed and continues to expand (Carey et al. 2015). Current geothermal development for electricity production in New Zealand utilizes reservoirs at depths up to ~ 3.5 km, dubbed the conventional resource. Future development of geothermal power in New Zealand aims at expanding the use of basement hosted geothermal resources, including the greywacke basement terranes of the North Island (Mroczek et al. 2016; Brathwaite et al. 2002; Wood et al. 2001), and newer discoveries proposed in the basement schist lithologies of the South Island (Sutherland

et al. 2017). Furthermore, future New Zealand geothermal potential lies in the development of deeper and hotter reservoirs likely hosted within similar basement lithologies (Bignall 2011; Sheburn et al. 2003).

In basement geothermal reservoirs hosted in greywacke or igneous rocks, fracture and fault networks control fluid flow (Wood et al. 2001; Sutherland et al. 2017; Wallis et al. 2012; Browne 1980). As such, these resources are susceptible to changeable heat fluxes (Aliyu and Archer 2021), dynamic fluid flow regimes (Graf and Therrien 2009), changes arising from mineral precipitation (McNamara et al. 2015), and tectonic stress fields (Davatzes and Hickman 2010), all of which can exert influence on the physical and mechanical properties of these fractured reservoir host rocks. Information on the physical and mechanical properties of basement rocks in New Zealand is thus crucial to their future development as geothermal resources both at conventional development depths and at novel, deeper depths. Furthermore, such dynamic environments generate fluid–rock interactions, which can alter the mineralogy and texture of reservoir host rocks, in turn modifying the physical properties, which govern their mechanical behaviour and subsequent structural network development (Siratovich et al. 2015; Heap et al. 2020a, b). In order to optimize and maintain structurally hosted geothermal resources, studies of their physical properties, their interactions, and their dynamic evolution due to fluid interactions need to be studied to understand the effects they produce in the subsurface reservoir (Gupta and Sukanta 2006; Di Pippo 2008; Grant and Bixley 2011).

To date, few data on the thermo-physical properties of New Zealand greywacke basement rocks exist (Richards and Read 2007; McNamara et al. 2014; Mielke et al. 2016). This study aims to enhance the understanding of the physical properties of these important geothermal reservoir rocks by presenting new data on the physical, mechanical, and elastic properties on the Waipapa greywacke terrane. This basement terrane is known to host geothermal reservoirs in the Ngawha Geothermal Field in Northland, and has the potential to host deeper geothermal resources in the Taupo Volcanic Zone (TVZ). Rock texture and microstructure analysis, combined with physical property determination (uniaxial compressive strength (UCS), tensile strength, triaxial compressive strength, static and dynamic elastic properties, porosity, density, seismic wave velocity, and permeability) of Waipapa Terrane greywacke samples presented here provide new information on the physical properties controlling brittle deformation in this lithology, the process necessary for it to act as a geothermal reservoir. Data presented here will contribute towards the improved construction of thermo-hydro-mechanical-chemical models of this basement terrane to assist in de-risking of future New Zealand geothermal systems and other similarly hosted geothermal reservoirs globally.

Geological setting

The Waipapa Terrane in New Zealand spans a significant portion of the northwest half of New Zealand's North Island, outcropping from the northwest border of the TVZ, and northwards into Northland (Fig. 1). Permian to Jurassic units comprise the terrane in a complex sequence of indurated and metamorphosed volcaniclastic sandstones and siltstones (Adams et al. 2009; Beetham and Watters 1985). Following Begg and Mazengarb (1996), in New Zealand the greywacke sequences are generally identified as medium to dark grey, coarse-to-medium grained, lightly

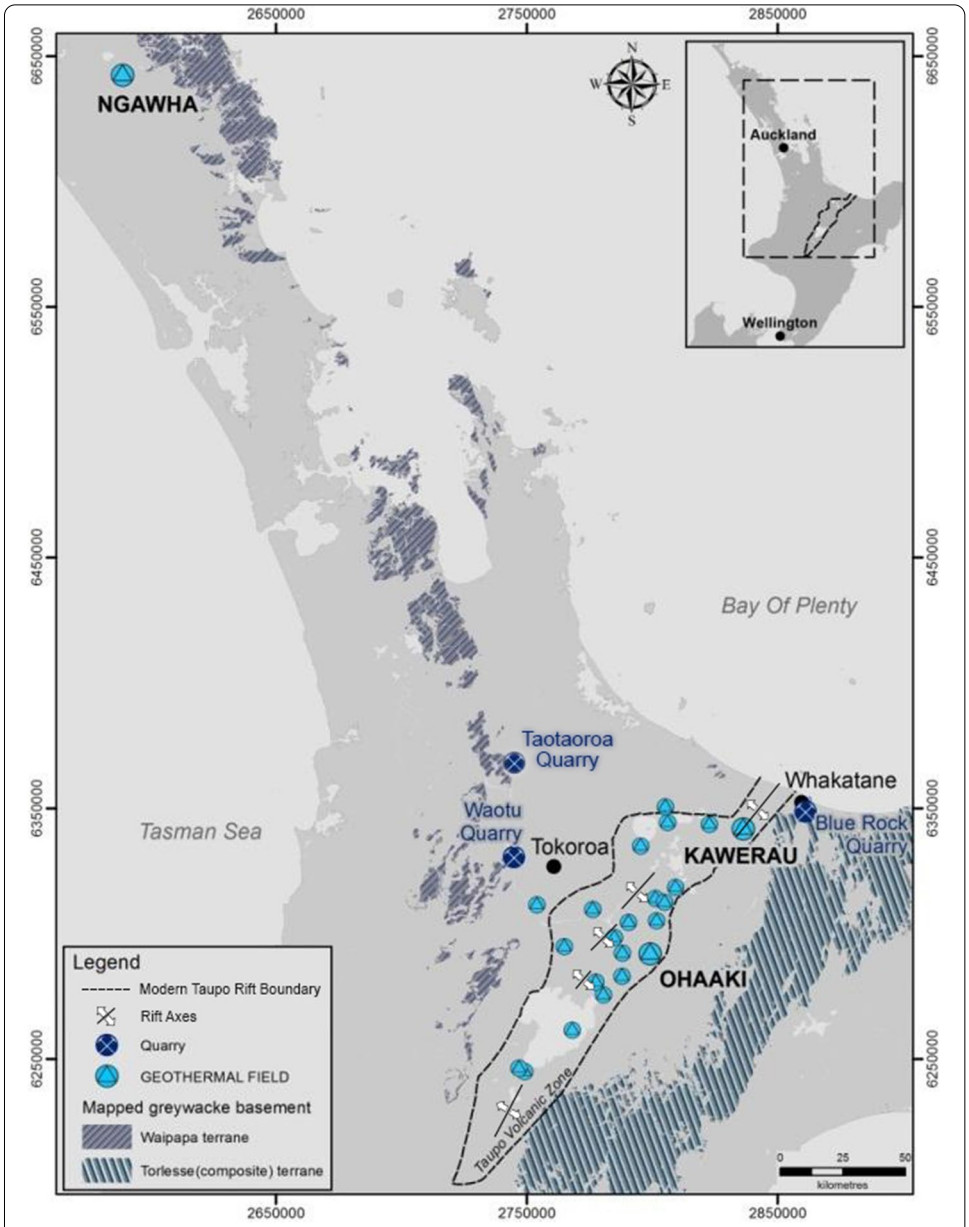

Fig. 1 Map of the North Island of New Zealand showing outcropping basement terrane rocks, major structural components of the TVZ, geothermal field locations, and the locations of the quarries used for sampling for this work. Modified from McNamara et al. (2014)

metamorphosed sandstones. Grains are poorly sorted and consist of angular quartz and feldspar, and lithic fragments of metamorphic and igneous rocks. The intergranular material consists of clay minerals formed during induration or low-grade metamorphism. Greywacke sandstones may be interbedded with lightly metamorphosed mudstones (argillite), usually layers of clay, silt, or mud, generally dark to black in colour, yet occasionally red when there is a high content of iron bearing minerals. The proportions between mudstone and sandstone are spatially variable within the Waipapa Terrane. Geothermal expression in this unit is well documented at the Ngawha

Geothermal Field in Northland, and potentially within the buried basement units underneath the modern (> 2 Ma) volcaniclastic deposits of the TVZ.

Locally, at the Ngawha Geothermal Field, Waipapa Terrane basement hosting the geothermal resource is composed of grey-green argillites and massive, quartzo-feldspathic greywacke sandstones which have experienced low-grade metamorphism [prehnite–pumpellyite grade (Mayer 1968)], and are strongly hydrothermally2011 altered and veined with common fault breccia textures (Bayrante and Spörli 1989; Cox and Browne 1998; Sheppard 1986). Waipapa greywacke basement is not yet drilled within the TVZ, an extensional intra-arc basin formed as a consequence of oblique subduction of the Pacific Plate underneath the North Island of New Zealand (Sheppard 1986; Wilson et al. 1995). Torlesse Terrane greywacke basement rock has been penetrated by drilling in the Kawerau, Ngatamariki, Ohaaki, Rotokawa, and Tauhara geothermal fields (Wood et al. 2001; Adams et al. 2009; Cole and Spinks 2009; Cant et al. 2018; McNamara and Massiot 2016; McNamara et al. 2016a, b; Bignall et al. 2010), and at Kawerau Geothermal Field hosts geothermal resources. The suture between the Waipapa and Torlesse terranes is thought to occur somewhere within the TVZ underneath the infill units but a precise location and depth is undetermined (Adams et al. 2009; Milicich et al. 2013a). However, given that seismic evidence points to brittle deformation reaching potential depths of ~ 6 to 8 km (Bibby et al. 1995), Waipapa terrane greywacke holds significant potential as a reservoir for hotter and deeper geothermal resources within the TVZ (Bignall 2011).

Limited data exist on the thermo-physical properties of the Waipapa terrane greywacke lithologies. UCS values of Waipapa terrane greywacke of ~ 193 MPa are recorded by Richards and Read (2007). McNamara et al. (2014) describe densities of ~ 2.71 g/cm^3, tensile strength ranges of 20–36 MPa, UCS values of 300–310 MPa, static Poisson's ratio and Young's moduli of 0.28 and 70 GPa, respectively, cohesion values of 51 MPa, a 0.93 coefficient of internal friction (μ), nuclear magnetic resonance porosities of 2%, and P-wave velocities (V_p) ranges of 6–6.25 km/s. Mielke et al. (2016) document similar values for the properties noted in McNamara et al. (2014) with the only exceptions being lower V_p values (~ 5.6 km s^{-1}), lower UCS values (123–245 MPa), and lower Young's modulus (~ 20–27 GPa). Connected porosity values of ~ 1%, permeability of $< 1 \times 10^{-16}$ m^2 (by using water as pore fluid), thermal conductivity (~ 2.5 Wm^{-1} K^{-1}) and diffusivity (~ $1.14–1.24 \times 10^{-6}$ m^2 s^{-1}), specific heat capacity of ~ 0.74–0.87 kJ kg^{-1} K^{-1}, and a shear-wave velocity (V_S) of 3 km/s are also recorded. All these tests were performed on dried samples.

Methods and materials

Materials and sample preparation

Samples of Waipapa greywacke terrane were acquired from quarry outcrops (Fig. 1) in order to test their physical and mechanical properties. Waipapa samples are sourced from Taotaoroa Quarry (TTGW), which is located between Cambridge and Matamata, ~ 8 km north of Karapiro Lake. While outcrops where samples are acquired show the Waipapa greywacke to be layered and fractured, the samples tested here contain no discernible anisotropy with respect to fabric. All the rock deformation data presented in this work were collected at the Rock Deformation Laboratory at the University of Liverpool (UK), and SEM (scanning electron microscope) images were collected using

a JEOL JSM 7001F FEG-SEM in the SEM Shared Research Facility, Albert Crewe Centre for Electron Microscopy at the University of Liverpool. Twenty-five, 20 mm diameter × 50 mm height, cylindrical specimens were cored and squared from samples of Waipapa greywacke sandstones from Taotaoroa Quarry. Squareness of the cored samples was better than 0.01 mm or less (Paterson and Wong 2015). Ten of these cores were then further cut into 20 mm diameter × 10 mm height disks and utilized for tensile strength measurements, and two of these cores had a macroscopic Mode I fracture created in it to use for single fracture permeability measurements. Three thin sections of Waipapa greywacke from Taotaoroa Quarry were made for petrological observations using an optical microscope. Finally, the sample taken to failure during triaxial testing was impregnated with epoxy resin and cut parallel to the core axis and perpendicular to the shear fracture plane, polished and utilized for imaging of the deformed specimen in an XL30 Philips scanning electron microscope (SEM).

Connected porosity measurements and bulk density

Connected porosity estimates are determined from cores using a helium multipycnometer (MVP-D160-E, Quantachrome Instruments). The connected porosity was calculated for 17 samples of Waipapa greywacke. Bulk density was calculated for three Waipapa greywacke cores, using their mass and solid volume.

Tensile strength

Brazilian tests, conforming to ATSM standards (ATSM D3967-08), were performed on 20-mm-diameter disks of dry greywacke basement rock, with a thickness-to-diameter ratio (t/D) between 0.2 and 0.75. Loading rate was kept at 0.2 MPa s^{-1}. Tensile strength is calculated with the following equation:

$$\sigma_t = \frac{2P}{\pi LD}, \tag{1}$$

where σ_t is the splitting tensile strength (MPa), P is the maximum force applied indicated by the machine (N), L is the thickness of the specimen (mm), and D is the diameter of the specimen (mm).

Uniaxial compressive strength

UCS experiments were carried out on ten dry greywacke samples from Taotaoroa Quarry. Axial and circumferential strain gauges were attached to the samples during testing. Samples were then brought to failure using a uniaxial press. The loading rate was not servo-controlled, but manually increased by ~ 0.2 MPa s^{-1} so that the tests lasted around 15 min. Static Young's modulus (E) and static Poisson's ratio (ν) are estimated from the gradient of a linear elastic region of the UCS test results (from 40 to 120 MPa).

Triaxial loading test

A single triaxial compressive test ($\sigma_1 > \sigma_2 = \sigma_3$) was carried out on a greywacke core in order to obtain the lithology's strength under confining pressure conditions of 20 MPa and a pore pressure of 5 MPa (effective pressure, $\sigma_{eff} = 15$ MPa) to ensure repeatability of results delivered in McNamara et al. (2014). Additionally, the evolution of permeability

and P- and S-wave velocity (V_p and V_s) were monitored to establish the development of these properties during loading to failure. We used a triaxial deformation rig able to perform triaxial experiments up to 250 MPa confining pressure (servo-controlled), with 250 MPa pore pressure (servo-controlled), and ~ 1000 MPa differential stress with a load capacity of 300 kN (Faulkner and Armitage 2013) (Fig. 2). Figure 2 shows the layout of this apparatus, illustrating where the sample is situated within the pressure vessel. It also shows the internal force gouge that provides high-resolution measurements of the axial force applied to the sample via a screw-driven actuator below the vessel.

V_p and V_s, and permeability measurements (by using water as fluid) of the sample are measured axially during this experiment. The position of the piezoelectric crystals (lead–zircon titanate) within the assembly is illustrated in Fig. 2. Axial loading proceeded at a displacement rate of 0.1 μm/s and paused at various intervals in order to obtain P- and S-wave velocity and permeability measurements (detailed in "Permeability measurements" section). The load point axial displacement reported is corrected for the

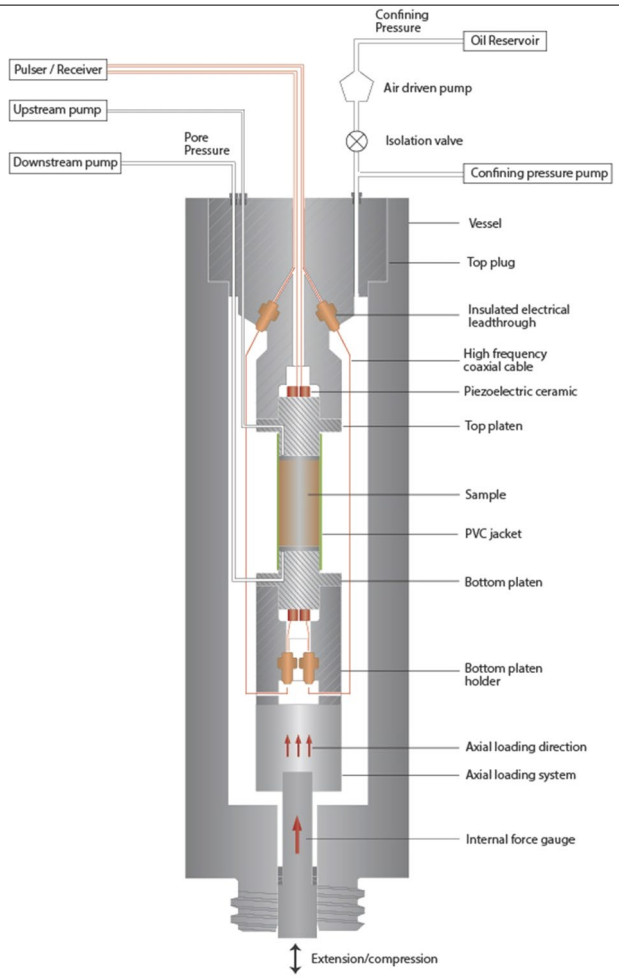

Fig. 2 A schematic illustration of the sample assembly contained within the pressure vessel used for the experiments described. It also highlights the position of the piezoelectric crystals within the assembly that are used for the P- and S-wave velocity measurements (Faulkner and Armitage 2013)

elastic distortion of the loading column, which is 75.5 kN mm^{-1} for the apparatus and so represents the axial displacement of the sample.

Elastic wave velocities and dynamic elastic moduli

Ultrasonic wave velocities (P- and S-wave) were measured along sample axes while loaded to failure in both uniaxial compression and triaxial testing (see Fig. 2 for rig design detail). These tests were carried out in order to understand how the wave velocities develop as microcrack networks develop under increasing stress, providing insight into the change in microcrack density in the samples during deformation (e.g. Schubnel et al. 2003). Values are determined under varying levels of axial stress during UCS testing, and under various levels of axial stress with constant confining pressures during triaxial testing. Physical property characterizations are summarized in Table 2.

Velocity data were used to calculate a dynamic Young's modulus (E_d) and dynamic Poisson's ratio (ν_d) for these samples, using the below equations and assuming isotropy (Kuttruff 1991):

$$E_d = \frac{\rho V_s^2 \left(3V_p^2 - 4V_s^2\right)}{V_p^2 - V_s^2}, \tag{2}$$

$$\nu_d = \frac{V_p^2 - 2V_s^2}{2\left(V_p^2 - V_s^2\right)}, \tag{3}$$

where ρ is the density (g cm^{-3}). The change in the bulk sample density, calculated from the variation in volumetric change which occurs during uniaxial compression, was accounted for in the analysis.

Permeability measurements

To examine fluid flow properties of the Waipapa Terrane greywacke, permeability tests were carried out on both intact samples and samples containing an induced Mode I single fracture. Permeability measurements were performed using the pulse-transient method (Brace et al. 1968) with deionized water used as the pore fluid. When the measurement begins, the upstream and downstream reservoir pressures of the sample are equilibrated and equal. A small increase (< 1 MPa) of the upstream reservoir pressure or a decrease of the downstream reservoir pressure is then imposed to apply a pressure gradient across the sample. The small pressure difference imposed was to avoid any adiabatic pressure changes that could result from a sudden larger pressure change (Brace et al. 1968). The decay characteristics of this pressure pulse, monitored in the upstream or downstream reservoir or both, may then be used to obtain a value for permeability.

Permeability measurements were made during triaxial compression tests to monitor permeability evolution as intact greywacke approaches failure. Permeability measurements were made for each pressure step (every 20 kN, or 63.91 MPa increase in load) and the loading piston was held stationary during the measurement. The first permeability measurement was taken at 0 MPa (no load applied) over a period of approximately one hour, with subsequent measurements made at compressive stresses of

20 kN (equal to 63.91 MPa load applied, over 3 h), 40 (127.81 MPa load applied, over 3 h), 60 (191.72 MPa load applied, over 4 h), 80 (255.62 MPa load applied, over 4 h), 90 (287.57 MPa load applied, over 4 h), 95 (303.55 MP load applied, over 4 h) and finally 100 kN (319.52 MPa load applied, over 2 h and 25 min) where brittle failure occurred. There is the possibility of continued deformation of the sample during the hold periods needed for permeability measurements. Any significant change in the pore volume could result in pressure transients that might affect the permeability measurements. However, the reduction in stress during the periods where permeability was measured was typically less than 1 MPa, which implies a very small increment of axial strain (~4 μm) given the stiffness of the apparatus is 240 MPa mm^{-1}. Furthermore, the pore volume was measured throughout the hold periods to a resolution better than 0.1 mm^3 indicating that negligible pore volume changes occurred during the times of the permeability measurements.

In order to understand how the permeability of single fracture responds to varying stress conditions, two intact greywacke rock cores (20 mm diameter × 10 mm height) were placed in a Brazilian loading jig, then loaded to failure in order to produce a single fracture plane (Nara et al. 2011). These samples were then carefully placed in a polyurethane jacket and put into a triaxial testing apparatus to hydrostatically load the specimen and measure evolving fracture permeability. For both specimens, permeability was recorded initially at 40 MPa confining pressure, with subsequent measurements taken every 5 MPa up to 110 MPa. After that, permeability measurements were taken at 120, 130 and 150 MPa. These confining pressures are chosen to reflect depths in crust that greywacke serves as a geothermal reservoir in New Zealand, with 40 MPa being the shallowest, ~1.6 km depth, and going as deep as 6 km (150 MPa) to represent potential deeper greywacke hosted geothermal systems (Bignall 2011; Sheburn et al. 2003). The procedure used here follows that of Nara et al. (2011). Connected porosity has not been estimated during the triaxial test, pore volume change can delineate the connected porosity evolution during the triaxial test.

Results

Petrology

From examination, Waipapa Terrane samples used in this study are composed of a medium-to-coarse grained (0.25–1.5 mm), greywacke sandstone consisting of abundant to common, subangular–subrounded, detrital quartz, plagioclase, and abundant lithic fragments (≤5 mm sizes) (Fig. 3). Lithic fragments are made of andesitic, basaltic, and rhyolitic lavas with granophyric textures, and siltstone. Some lava lithics show a trachytic texture. The greywacke sandstone is clast supported and matrix poor (Fig. 3A, B, F). Matrix is composed of indurated clay/silt. Chlorite, calcite, quartz, and occasional epidote are found as vein minerals. In general, the Waipapa samples are moderately altered to chlorite, leucoxene and clay with some weak epidote alteration. Plagioclase crystals in places are weakly altered to clays while detrital biotite crystals are relatively fresh. Within the rock andesite lithic fragments show some albitization. The groundmass is altered to chlorite and detrital plagioclase is partially altered to clay. Mineralization within observed microfractures in these samples indicates that these crack networks at one point operated as fluid flow pathways (Fig. 3C–E).

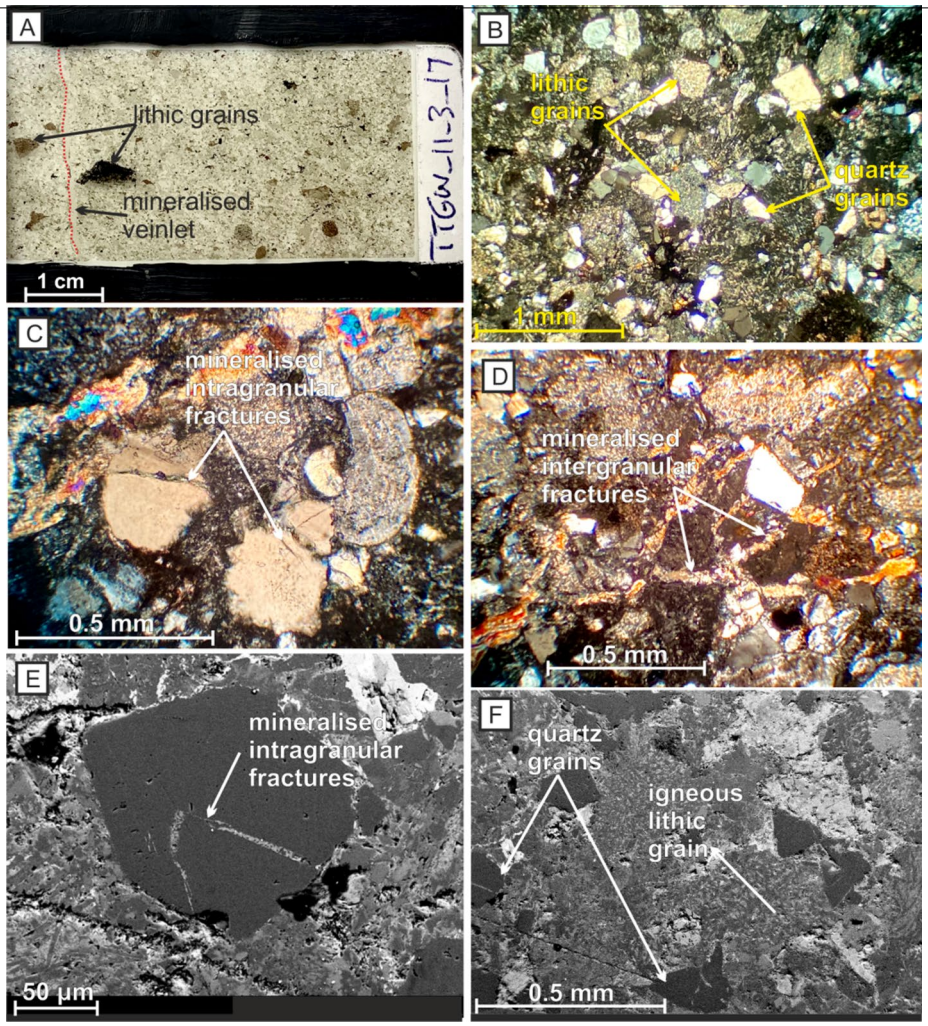

Fig. 3 **A** photograph of thin section of sample TTGW_11_3_17 showing grain size variation and mineralized veinlets (red line); **B** photomicrograph (XP; TTGW_11_3_17) showing typical grain size and texture of Waipapa basement greywacke; **C** photomicrograph (XP; TTGW_11_3_17) showing mineralized intragranular fractures in quartz grains; **D** photomicrograph (XP; TTGW_11_3_17) showing mineralized intergranular veinlets in Waipapa greywacke; **E** SEM backscatter image (TTGW_11_3_17) showing mineralized intragranular fractures within a quartz grain; **F** SEM backscatter image (TTGW_11_3_17) showing typical grain sizes and textures of Waipapa greywacke basement and the igneous textures noted in lithic grains. Qz = quartz, Pl = plagioclase

Greywacke samples also show a small amount of microcracks with an estimated crack density parameter of 0.51 using the methodology of O'Connell and Budiansky (1974). This method was applied using the relation for saturated materials containing circular cracks and using the Poisson's ratio of the uncracked material (taken to be that above crack closure at 40 MPa of axial stress) along with the Poisson's ratio before loading commenced.

Connected porosity and bulk density

Table 2 provides an overview of the mechanical (tensile and unconfined compressive strength), elastic, and physical properties of intact Waipapa greywacke.

Tensile strength

A standard deviation in tensile strength for the Waipapa greywacke samples indicates some variability (Table 2), which is not outside the norm for these types of experiments (Gale and Holder 2008).

Uniaxial compressive strength (UCS) and static elastic moduli

For all UCS tests (Table 1), stress–strain curves show a slight concave-upwards trend at low loads, followed by a linear region up to failure (Fig. 4). No discernible yield point was observed before failure. Static Young's moduli range between 54 and 85 GPa and static Poisson's ratios range from 0.19 to 0.36 (Table 2).

Triaxial compressive strength

Permeability measurements (Table 1) performed prior to the start of the triaxial test provide an intact rock permeability of $1.65 \cdot 10^{-21}$ m^2. Axial loading proceeded at a displacement rate of 0.1 microns/s, and the loading was stopped at regular intervals in order to obtain P- and S-wave velocity and permeability measurements (Fig. 9). The axial displacement reported is corrected for the elastic distortion of the loading column which is 180 kN/mm for the apparatus.

We consider the sample to be drained during the triaxial test. Although the permeability is low, the characteristic time ($t = l^2/k$) for fluid diffusion is calculated to be on the order of ~ 40 min, given the sample length and approximating the sample storage capacity to be $4 \cdot 10^{-12}$ Pa^{-1} (porosity multiplied by fluid compressibility; see Faulkner et al. 2018). This value corresponds reasonably well to the time taken for the permeability measurements and suggests that the timescale over we ran the experiment, and the strain rate used, meant that the sample was drained during the test.

The loading curve in Fig. 5 shows a typical, though short, initial concave-upwards trend, then quasi-linear loading, the slope of which provides a static Young's modulus of ~ 55 GPa. No yield is observed as failure (314 MPa) is approached, and the sample fails while still under quasi-linear loading. Reloading of the sample after failure occurs along a shallower gradient indicating the fractured sample is more compliant, and a residual strength of ~ 120 MPa is recorded.

Throughout the triaxial test, as strain accumulates before failure is reached (Fig. 5), the permeability does not vary greatly. The small changes observed up to displacements of ~ 0.42 mm are likely a result of measurement variability. Only immediately before failure is a dramatic increase in permeability seen, where the permeability increases by ~ 4 orders of magnitude. During this part of the loading history, the pore volume shows a decrease of 2.73 mm^3 (Fig. 6). Most of this decrease occurred during the initial loading of the sample.

Following failure and unloading of the sample, the permeability is much lower than seen at peak stress. Following residual strength yield, and a small amount of shearing along the shear fracture created during loading, the permeability increases slightly again, although this change is within the uncertainty bounds of our permeability

Table 1 List of samples examined in this study and the experimental tests performed on each

Sample	Uniaxial	Triaxial	Brazilian	V_p–V_s	C. porosity	Permeability	SEM	XPL	SF	Density
TTGW_11_3_H1160								✓		
TTGW_11_3_H1161								✓		
TTGW_11_3_4_triax		✓		✓	✓	✓	✓	✓		
TTGW_11_2_1	✓									
TTGW_11_2_2	✓									
TTGW_11_2_3	✓									
TTGW_11_2_4	✓									
TTGW_11_3_1					✓					
TTGW_11_3_2					✓					
TTGW_11_3_3					✓					
TTGW_11_3_5					✓	✓ (× 18)			✓	
TTGW_11_3_6	✓				✓					
TTGW_11_3_7					✓					
TTGW_11_3_8			✓ (× 3)		✓					
TTGW_11_3_10				✓	✓					
TTGW_11_3_11	✓									✓
TTGW_11_3_12	✓			✓						✓
TTGW_11_3_13	✓			✓						✓
TTGW_11_3_14	✓			✓						
TTGW_11_3_16					✓					
TTGW_11_3_17					✓	✓ (× 18)	✓		✓	
TTGW_11_3_18			✓ (× 3)		✓					
TTGW_11_3_19					✓					
TTGW_11_3_20			✓		✓					
TTGW_11_3_21			✓		✓					
TTGW_11_3_22					✓					
TTGW_11_3_23			✓ (× 2)		✓					

TTGW Taotaoroa quarry greywacke, *SF* single fracture experiment. Numbers in brackets (e.g. (× 3)) indicate the number of times that test was carried out on that sample. Samples TTGW_11_3_H1160 and TTGW_11_3_H1161 are thin sections

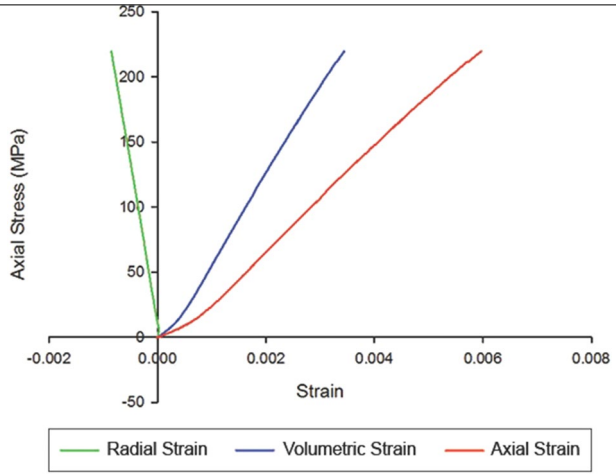

Fig. 4 Stress–strain curves obtained from the uniaxial test of the Waipapa greywacke sample TTGW_11_2_2. These results are typical of the UCS tests in general

Table 2 Summary of the measured physical properties of Waipapa greywacke from this study

Property	Measured range	# of tests	Mean	Standard deviation
Tensile strength (MPa)	14.4–32.42	10	21.07	8.28
UCS (MPa)	205–384	10	285.6	60.17
Poisson's ratio (ν_S)	0.19–0.36	10	0.316	0.1
Young's modulus (E_S) (GPa)	54–85	10	72.8	9.04
Poisson's ratio (ν_D)	0.28–0.30	3	0.29	0.01
Young's modulus (E_D) (GPa)	80–84	3	81.7	2.08
Bulk density (ρ) (g cm^{-3})	2.721–2.731	3	2.726	0.0051
Connected porosity (ϕ) (vol%)	0.841–1.304	17	1.035	0.152

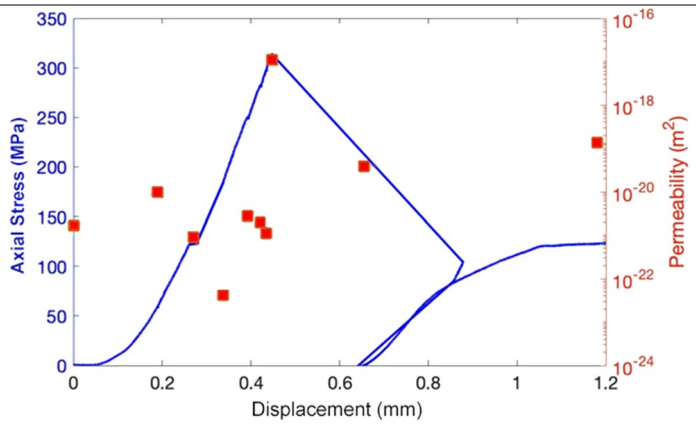

Fig. 5 Results from the triaxial loading experiment. The blue line shows loading of the sample to failure, followed by unloading and reloading the sample with the shear fracture to residual failure. The red squares show the evolution of permeability during the loading history

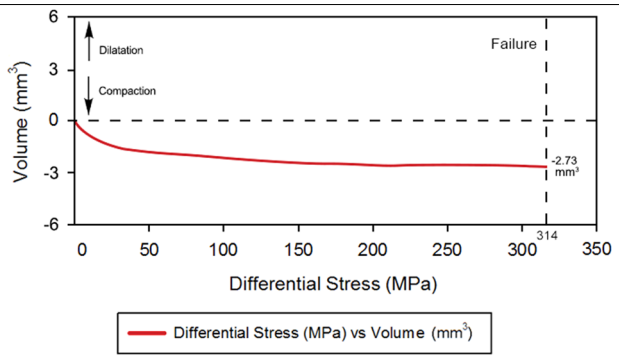

Fig. 6 Pore volume change with increasing differential stress during the triaxial test

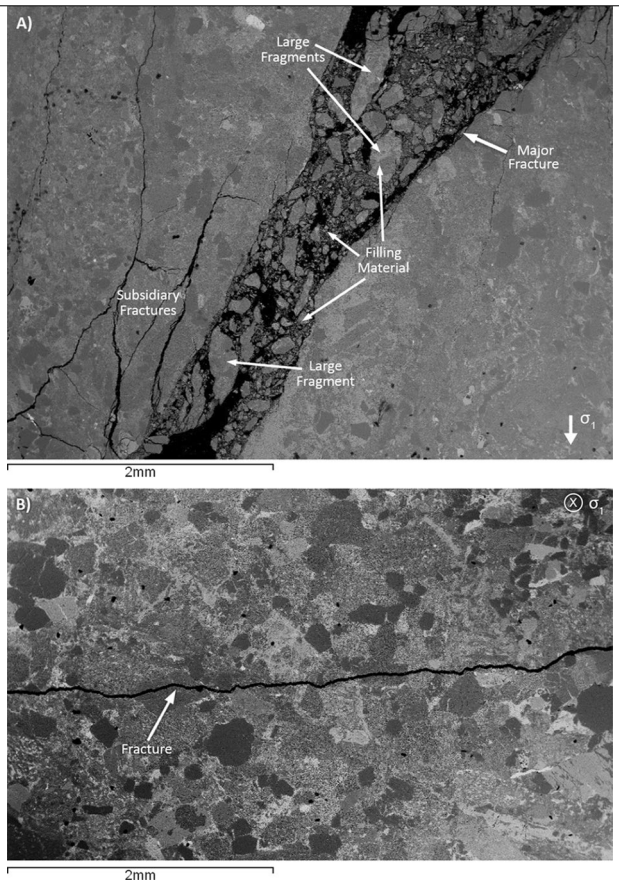

Fig. 7 **A** SEM image of the greywacke sample TTGW_11_3 brought to failure in triaxial conditions. The deformed sample was mounted in epoxy resin and cut and polished for imaging within the SEM. This image displays the shear fracture and its filling material. A microfracture network is visible to the left side of the primary shear fracture. **B** SEM image shows an induced Mode I fracture in a greywacke disk (TTGW_11_3_17) using the Brazilian jig. The fracture is both intergranular and intragranular

measurements. The shear fracture makes an angle of approximately 30° to the cylinder axis. A photo of the final deformed sample can be found in Additional file 1: Fig. S1.

Scanning electron microscopy observations

SEM observations (Table 1) of the shear fracture generated by the failure of the core during the triaxial test reveal it is filled with fragments of greywacke material (Fig. 7a). The upper extremity of the fracture, where the sample comes into contact with the loading platen, widens and has a triangular shape, filled with large greywacke fragments ($\leq$0.675 mm) set in a finer matrix ($\leq$200 µm sized cement grain). The typical aperture of the fracture is < 1 mm. A network of subsidiary fractures develops close to both sides of the main rupture. This subsidiary fracture network is variable and includes both relatively wide fractures and clusters of narrower cracks. The subsidiary fractures have variable morphologies that are broadly parallel and sub-parallel to the main fracture, and parallel to the loading direction. Very few subsidiary brittle deformation features are observed at greater distance from the main rupture in the tested sample.

The synthetically produced fractures from Brazilian loading (Fig. 7b) show very little comminution and, in contrast to the shear fracture (Fig. 7a), few fragments contained within the fracture. Fracture walls are a mixture of tortuous and straight, and rough and smooth, and the fracture width is consistent (~25 µm). There is no development of a damage zone or subsidiary fractures around the main fracture (Fig. 7b). Similar post-failure conditions occurred for TTGW_11_3_5 sample (Fig. 10). Still, in Fig. 7b it is visible how the fracture formed is both intra- and inter-granular. Clearly there is a preference for development of the fracture through the matrix along grain boundaries more than through the grains, as the matrix is a weaker material, however the brittle failure undoubtedly affects both grains and matrix.

V_p, V_s, and dynamic elastic moduli

V_p and V_s values were acquired during both uniaxial and triaxial tests (Table 1). The P-wave and S-wave data were measured along the sample axis. From uniaxial tests, V_p

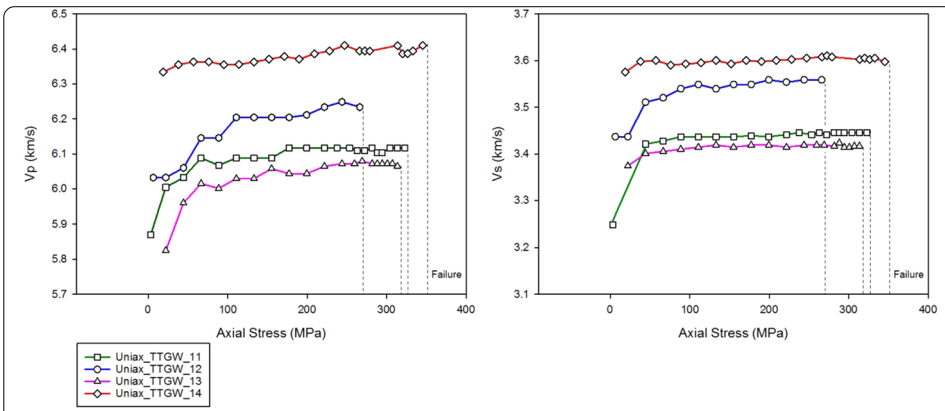

Fig. 8 Seismic wave velocities (V_p and V_s) measured along the sample axis during uniaxial compressive tests

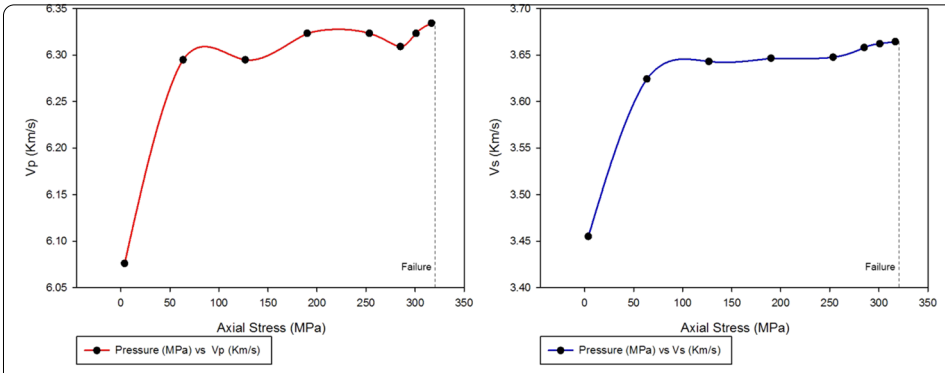

Fig. 9 Seismic wave velocities (V_p and V_s) measured during triaxial compressive test

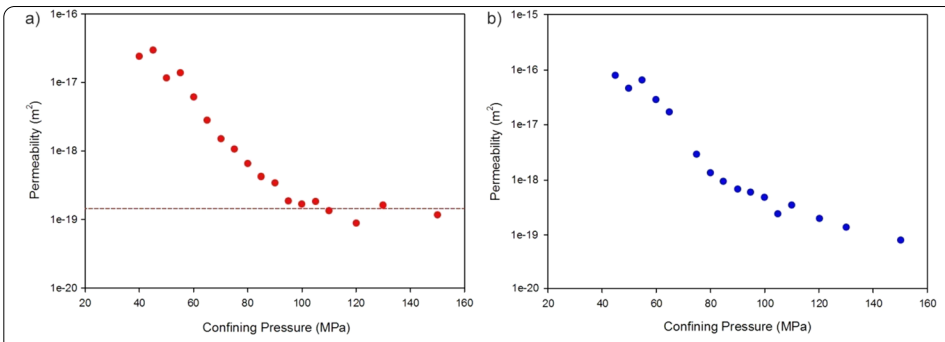

Fig. 10 Graphs of permeability against confining pressure through a single fracture (samples TTGW_11_3_5 (**a**) and TTGW_11_3_17 (**b**)). Red dashed line indicates where permeability becomes stable. Overlapped graphs 10a and 10b are shown as Additional file 2: Figure S2, Additional file 3

varies from 6.072 to 6.410 km s^{-1} (Fig. 8), and V_s varies from 3.423 to 3.605 km s^{-1}. From the triaxial test, peak V_p is 6.334 km s^{-1} and peak V_s is 3.647 km s^{-1}. Dynamic Poisson's ratio was in the range of 0.28—0.30 and dynamic Young's modulus was in the range 80 to 84 GPa.

Figure 8 shows the trend of V_p and V_s for Waipapa greywacke during uniaxial testing. Data show an initial rapid increase in V_p and V_s as the differential stress is increased (Fig. 8). After that, V_p and V_s assume a sub-horizontal trend and show little changes up to the point of failure. In detail, all the V_p curves show fluctuation with a general increasing trend, while, for the V_s, in the beginning the trend is upward, then it levels out until failure. Data from the triaxial test reveal a similar trend between V_p, V_s, and axial stress (Fig. 9).

Single fracture permeability

As confining pressure increased a monotonic decrease in permeability is observed for the single, Mode I fracture in Waipapa greywacke (Fig. 10). In both experiments, a similar trend in permeability response is observed, with permeability measurements (Table 1) between 10^{-16} m^2 and 10^{-17} m^2 made at 40 MPa confining pressure, and

permeability measurements of ~ 10^{-19} m^2 made at 150 MPa confining pressures. At no point in the experiments did the fracture cease to allow the transmission of fluid along it. We saw that even with 150 MPa confining pressure the permeability was still higher than measured for the intact samples (Fig. 10 and Additional file 2: Figure S2).

Discussion

The physical properties of a lithology affect its ability to transmit fluid within it. The matrix permeability of a rock is the key factor influencing fluid flow in a rock type, which in turn is strongly influenced by porosity, pore connectivity and, for low-porosity lithologies, microfractures. Beyond matrix permeability a lithology's ability to transmit fluid is dictated by the presence of structures (Evans et al. 2005), and the formation of structural permeability within a lithology is related to the mechanical properties of the rocks that constitute it. We discuss here our findings in the context of how they help understand fluid flow within Waipapa greywacke basement units.

The role of microfractures in Waipapa greywacke mechanical strength

The Waipapa greywacke mechanical strength reported here is high. As a comparison, the mechanical strength of the Waipapa greywackes (Table 3) is higher than that found in other lithologies reported as mechanically strong such as Westerly granite [UCS strength ~ 200 MPa (Mitchell and Faulkner 2008; Heap and Faulkner 2008)], or the Rotokawa Andesite, another important geothermal reservoir rock in the TVZ (UCS strength of 60–211 MPa; Siratovich et al. 2012, 2014).

In Waipapa greywacke porosity ranges from 0.841 to 1.304% (Table 3). These measurements of low porosity, coupled with the microstructural observations such as optical microscope (Fig. 3) illustrate the minimal primary porosity that exists within this lithology. The presence of microcracks in a low-porosity lithology often contribute little to the overall porosity, but can have an important impact on its mechanical strength, and thus the stresses at which it will experience brittle failure (Siratovich et al. 2014; Eberhardt

Table 3 A comparison of the physical and elastic properties values for Waipapa greywacke samples (*TTGW* Taotaoroa Quarry; *WAGW* Waotu Quarry) measured in this study [this study; McNamara et al. 2014) and Torlesse greywacke (this study (connected porosity); McNamara et al. 2014; Stewart 2007), Rotokawa andesite (Siratovich et al. 2012, 2014)

Property	TTGW (this study)	# of tests	WAGW	# of tests	Rotokawa andesite	# of tests
Tensile strength (MPa)	14.4–32.42	10	20.3–35.7	8	9.99–24.13	12
UCS (MPa)	205–384	10	301–310	2	60–211	22
Poisson's ratio (ν)	0.19–0.54	10	0.28–0.29	2	0.09–0.34	22
Young's modulus (E) (GPa)	54–85	10	65–70	2	20–44	22
Poisson's ratio (ν_d)	0.28–0.30	3	–	–	0.13–0.23	22
Young's modulus (E_d) (GPa)	80–84	3	–	–	25–46	22
Density (ρ) (/cm^{-3})	2.727	3	2.71	2	2.49	22
Connected porosity (ϕ) (vol%)	1.035	17	~ 2	2	8.44	22

Mean values are reported for density and connected porosity. Dynamic properties are identified in this table with the subscript "*d*" (E_d and ν_d)

et al. 1999; Faulkner et al. 2006; Lajtai 1998). Previous studies on low-porosity crystalline rocks have shown that the presence of microfractures is evident by deviation from linear elastic behaviour at stress levels well below the failure stress, as well as an increase in volumetric strain (Mitchell and Faulkner 2008; Zoback and Byerlee 1975). Both these observations lend support to the interpretation that, as loading progresses, existing microfractures start to propagate, leading to reduced compliance (related to deviation from linear elasticity) and volumetric strain increase.

Microstructural observations of microcrack densities of 0.51, in addition to the low-porosity measurements, are likely related to the initial short "tail" on the triaxial experiment stress–strain graph, as they are closed up during initial loading. The loading curve (Fig. 4) indicates little evidence for dilatancy from the volumetric strain curve and there is an appreciable lack of any yield point. This indicates that the formation of any microcrack network prior to failure is very limited, and contrasts with other brittle deformation studies on low-porosity rock which show evidence of microcrack formation prior to failure (Mitchell and Faulkner 2008; Eberhardt et al. 1999; Zoback and Byerlee 1975). Moreover, the direct dilatancy measurements made via volumometry during the triaxial test also indicate little or no dilatancy prior to failure, though similar direct dilatancy measurements made during the brittle deformation of low-porosity anhydrite indicate dilatancy can occur and thus potentially affect sample porosity and permeability during deformation prior to failure (De Paola et al. 2009).

Elastic wave velocities can be strongly attenuated by the presence of microcracks in crystalline rocks (Siratovich et al. 2014; Vinciguerra et al. 2005; Blake et al. 2012; Heap et al. 2014) such that microcracking can strongly reduce V_p and V_s. The mechanical test results from the Waipapa greywackes show, at the beginning of both the UCS tests and the triaxial loading test, there is a short-lived V_p and V_s increase. This finding is similar to findings on wave velocities measured during pressure increase on low-porosity basalts (Fortin et al. 2011). We suggest this short-lived V_p and V_s increase represents closure of the low microcrack density present in the intact greywacke sample. Further changes in V_p and V_s with increasing pressures are minimal and, importantly, show no appreciable decrease immediately before failure that might indicate the development of a microcrack network (Figs. 4, 8).

The lack of microcracks within intact Waipapa greywacke is interesting given this lithology is heavily fractured in situ. It may be that brittle damage is very localized around macrofractures, as we observed in our failed sample from our triaxial deformation experiment here (Fig. 7). Reloading of the failed sample shows a much shallower gradient than initial (pre-failure) loading, indicating that the Young's modulus has appreciably decreased and the fractured sample is much more compliant, consistent with the presence of a larger population of microcracks, particularly in the near vicinity of the microfracture.

Waipapa greywacke permeability

The results given in Table 2 are comparable to previous measurements on connected porosity of Waipapa greywacke (Mielke et al. 2016), and connected porosity and permeability measurements made under the same conditions for Torlesse greywacke [$\sim 1.6\%, \sim 4.824 \cdot 10^{-22}$ m^2 (McNamara et al. 2014)], which also hosts geothermal

reservoirs (Milicich et al. 2016). These greywacke lithologies display the lowest porosity and permeability values measured to date across a range of New Zealand geothermal lithologies. For comparison, Rotokawa andesite has permeability values four to five orders of magnitude greater than the greywacke units ($\sim 10^{-17}$ m^2) (Siratovich et al. 2014), and greater porosity values (Table 3), while lithologies from the Tahorakuri Formation, Matahina ignimbrite, Te Teko Formation, Tahuna Formation, and a range of TVZ andesite, dacite, and rhyolite lavas all have higher average porosity values (Mielke et al. 2016; Wyering et al. 2014).

The low porosity range reported here for Waipapa greywacke suggests a low density of inherent microstructures in this lithology, and those that are present are minimally connected. This is supported by the low permeability measurements ($1.65 \cdot 10^{-21}$ m^2), the low reduction in volume observed under triaxial deformation experiments, and SEM images reported in this study. The evidence and arguments presented here for the low microfracture density of intact Waipapa greywacke have implications for the matrix permeability of this rock. The microcrack density does not have a great influence on the porosity, but the permeability is strongly affected by the presence of microcracks (Costa 2006; Chaki 2008), though this is strongly dependent on effective stress levels and whether the rock undergoes brittle failure or not (Faulkner and Armitage 2013; Zoback and Byerlee 1975).

In this study, Waipapa greywacke displayed no sign of significant dilatancy during deformation experiments (Figs. 4 and 6), and a lack of decrease in V_p and V_s before failure in both uniaxial and triaxial tests. This is complemented by the absence of enhanced permeability observed during loading to failure in the triaxial deformation experiment (Fig. 5).

It has been well demonstrated that faults and fractures in brittle rock are produced by the interaction and fusion of many microcracks (Mitchell and Faulkner 2008; Lockner et al. 1991; Lockner et al. 1992; Reches and Lockner 1994; Healy et al. 2006). When differential stress is applied to an intact rock sample, microfractures damage increases as the rock approaches failure, and the resultant increasing dilatancy will have direct impacts on both porosity and permeability. For example, permeability increases in Westerly Granite as it is triaxially deformed are recorded as the granite failure strength is approached due to increasing development of microcracks, which then increases further as stress is relaxed allowing more connectivity between variable oriented microcracks in the rock (Mitchell and Faulkner 2008; Zoback and Byerlee 1975). Even for the anhydrite it has been demonstrated that under triaxial conditions, after an initial compaction, dilatancy occurs producing an increase of porosity and permeability (De Paola et al. 2009). Instead for a diagenetically different rock like basalt, characterized by elevated porosity, increasing the effective pressure a constant decreasing in permeability and crack density takes place, drawing a quite logarithmic curve (Fortin et al. 2011). In this study, Waipapa greywacke displayed no sign of dilatancy during deformation experiments, both uniaxial and triaxial (Figs. 4 and 6), similar to results reported in McNamara et al. (2014). This lack of dilatancy signal in our experiments is supported by the lack of decrease in V_p

and V_s before failure in both uniaxial and triaxial tests, and a lack of increased permeability observed during loading in the triaxial deformation experiment (Fig. 5). In terms of macrofracture generation within intact Waipapa greywacke, it appears that dilation of axially aligned microcracks and their subsequent coalescence must occur immediately before failure such that their impacts on other property measurements are not captured by our experimental work here. Concerning the contributions pre-failure deformation makes to Waipapa greywacke permeability, we conclude this is likely to be small, though suggest future experiments of this nature be performed at higher resolution along the stress–strain path. Our results suggest that Waipapa permeability is dominated by macrostructures, as no permeability is witnessed to be generated by dilatancy effects from deformation in this lithology, agreeing with similar conclusions made elsewhere (McNamara et al. 2014).

Passelègue et al. (2018) demonstrate that permeability anisotropy is caused when the intact rock is loaded to macroscopic failure though the rock being deformed is essentially isotropic, indicating that permeability anisotropy begins to evolve only after a lithology is deformed, and that anisotropy will be aligned with respect to the stress state that generated the fractures. Considering the low permeability of intact Waipapa greywacke, permeability anisotropy is expected to be an important aspect of this lithology as a geothermal reservoir. Experimental data presented here confirm the introduction of permeability anisotropy within Waipapa greywacke. Rapid, large increases in permeability (around four orders of magnitude, from 10^{-21} m^2 to 10^{-17} m^2) at the point of brittle failure are noted from the triaxial compression experiment (Fig. 5) and the single fracture permeability tests (Fig. 10). Thus, permeability dramatically increases in Waipapa greywacke rocks as a result of brittle deformation, implying an anisotropic permeability will develop, oriented with respect to a given stress field.

Defining the orientation of such permeable anisotropy in Waipapa greywacke is not simple given the complex nature of the tectonics associated with this lithology in geothermal regions (McNamara et al. 2019). Within the TVZ the Waipapa greywacke is subject to NW–SE directed extension, with local variations (McNamara et al. 2019). Under contemporary tectonic conditions, fractures generated in Waipapa greywacke will predominantly align to this stress state (striking NE–SW, parallel to σ_2), thus defining the permeability anisotropy. However, the Waipapa greywacke has undergone deformation prior to TVZ rifting resulting in previous brittle deformation in a range of orientations (Rowland and Sibson 2004). We suggest that lateral permeability anisotropy in Waipapa greywacke will be aligned to the strike of the TVZ rift (NE–SW), in which both brittle structures formed during rifting, and brittle structures formed pre-rifting, but preferentially aligned for slip in the current stress field, control geothermal fluid flow. Indeed, a dominant NE–SW fracture strike orientation is shown within fluid flow zones in geothermal wells drilled into Torlesse greywacke basement at the Kawerau Geothermal Field (Wallis et al. 2012), establishing these fracture patterns do exist in greywacke basement type lithologies in the TVZ. Implications of our findings for geothermal fluid flow in the Waipapa greywacke reservoir Ngawha Geothermal Field are more difficult

to determine due to a lack of direct structural or stress information from this location (Mongillo 1985). Reported structures have E–W, and NE–SW strike orientations and are associated with NW–SE directed extension in the region (Bayrante and Spörli 1989). Assuming this structure-stress arrangement, we can infer from out experimental results that a macrofracture related permeability anisotropy aligned NE–SW would form in the Waipapa basement of the Ngawha Geothermal Field.

In a geothermal reservoir where permeability is controlled by macrostructures, such as those in Waipapa greywacke, the ability for brittle structures to maintain fluid flow is important to the resource longevity and sustainability. This study examined the effect of single macrofracture behaviour on the permeability of Waipapa greywacke. Macrofracture closure pressures of synthetically generated fractures in Waipapa greywacke falls between 95 to 112 MPa. At these closure pressures, fluid flow across the fracture was observed to continue, developing a stable permeability around 10^{-19} m^2 for confining pressures between 95 and 150 MPa (Fig. 10). Thus, even at closure, macrofractures in the Waipapa greywacke provide continued permeability (2 orders of magnitude higher than intact greywacke permeability). Permeability measurements on fractured greywacke under triaxial conditions also support persistent permeability in greywacke fractures post initial failure (Fig. 5). Similar large increases in permeability from inducing a single fracture are reported from dense volcanic rocks in geothermal regions (Lamur et al. 2017). Persistent permeability in Waipapa greywacke fractures under closure pressures may be facilitated by incomplete fracture closure due to the presence of fragments inside the fractures propping it open, asperity generation, permeability via secondary brittle damage generated around the main brittle fracture (Fig. 10). Our observations suggest all three possibilities may contribute in some way. A size range of wall rock fragments are observed within the triaxial fracture experiment, some of which are likely more than significant to prop open a newly generated fracture and facilitate ongoing fluid flow within it. The longevity of this propping is uncertain, as over time with ongoing fracture slip, these fragments may be constantly reduced in size and maintain less open space. With enough time and comminution of fracture fill material, combined with fluid–rock interaction, gouge may be generated and potentially seal the fracture completely to fluid flow. Asperity generation in fractures tested here will certainly play a role in ongoing fracture permeability after closure pressures are reached, as morphologically different fracture walls are observed in fractures generated in both triaxial and tensile tests. As with grain propping, there is a time limit to the ability for asperity to maintain fluid flow in a fracture as consistent slip will eventually grind these asperities down. The exact contribution secondary brittle damage makes to observed greywacke permeability is unknown, which makes it difficult to address in terms of their contribution to permeability under closure pressures. Given these secondary structures generated under the same experimental conditions as the primary brittle failure it is reasonable to assume they would behave similarly to the main fracture, though given their more varied orientation with respect to σ_1, and the high level of intersection observed this is questionable and requires further study.

It should be noted that the results from the measurements on the single fracture are represented in terms of permeability to allow direct comparison with the permeability of the intact rock, as has been done in previous studies (Heap and Kennedy 2016; Wang et al. 2016; Pérez-Flores et al. 2017; Kushnir et al. 2018; Eggertsson et al. 2020). Strictly, reporting permeability for fracture flow is not correct, as the calculation assumes that fluid flow occurs over the cross-sectional area of the specimen, whereas for rocks with a low matrix permeability, fluid will predominantly flow through the fracture. Consequently, the "permeability" becomes scale dependent (Heap and Kennedy 2016). This can be illustrated by considering that if the sample diameter were doubled, the flow would also double, as the length of the fracture has increased by a factor of two. However, the cross-sectional area used in the permeability calculation would quadruple and the permeability would appear to half for the larger specimen. Hydraulic transmissivity, the product of the fracture permeability and its thickness, is a better way to represent the flow properties of fractures. This parameter cannot be directly derived from our pulse-transient measurements we made (Rutter and Mecklenburgh 2018) and could only be estimated by approximating the average aperture of our fractures. Given the uncertainty in the fracture aperture estimation, we did not make this calculation.

In summary, intrinsic microfracture density in Waipapa greywacke is low, and the development, coalescence, and growth of the microfracture network before failure is minimal. Consequently, microfractures play a key role in the formation of permeable structures within the Waipapa greywacke lithology only in proximity of the brittle failure, immediately prior of the pick stress. Macrofractures demonstrably increase permeability in Waipapa greywacke, contribute to long-lived permeability post-failure, and the permeability they develop within this lithology is anisotropic, and so permeability vectors in the greywacke units will be related to the local and regional stress conditions.

Conclusions

Our experiments indicate a high mechanical strength for intact Waipapa greywacke lithology that is partly due to a low density of inherent microcracks. This lack of microcracks contributes to the low intrinsic porosity and permeability of intact Waipapa greywacke. Our experiments confirm that the Waipapa greywacke lithology will only support fluid flow via the generation of macrostructures. Furthermore, these macrofractures maintain a level of permeability after stress conditions relax (fracture closure). Brittle fractures generated in Waipapa greywacke thus remain important permeable components in this lithology for an undetermined length of time after their formation. Such macrofractures controlled permeability is inherently anisotropic and as such the directionality of fluid transmission in the Waipapa greywacke will be strongly controlled by the arrangement of the local tectonic stress field as this controls orientation of microfractures development. Given that structures impart strong permeability anisotropy to Waipapa basement, any fluid flow modelling of geothermal systems within such geological units should account for this. Further studies on Waipapa greywacke mechanical strength that simulate deeper crustal levels, and flow experiments through single

macrostructures under such conditions are required to better quantify the fluid flow properties of this basement lithology needed for accurate modelling.

Supplementary Information

The online version contains supplementary material available at https://doi.org/10.1186/s40517-022-00218-2.

Additional file 1: Figure S1. Triaxial deformed sample: 20 mm diameter × 50 mm height cylindrical specimen cored and squared from a rock sample of Waipapa greywacke sandstone from Taotaoroa Quarry (New Zealand), identified as TTGW_11_3_4_triax, utilized during the triaxial test and permeability measurements. This sample presents an induced fracture due the failure during triaxial test. After the failure the sample has been submerged by epoxy resin in order to maintain intact the rock for further studies.

Additional file 2: Figure S2. Graph of permeability against confining pressure through a single fracture for samples TTGW_11_3_5 (Fig. 10a) in red and TTGW_11_3_17 (Fig. 10b) in blue. The graph shows similar trends between the two samples. Red dashed line indicates where permeability becomes stable.

Additional file 3: Figure S3. An example of one of our lowest permeability measurements at ~ 0.25 mm displacement (see Fig. 5). The data illustrate that we use only the initial part of the pressure decay to determine permeability but the natural logarithm of the difference between the pressure and the final pressure plotted against time still gives linear trend that can be used to determine the permeability.

Acknowledgements
We thank Julian Mecklenburgh for discussions of research results. We acknowledge the research staff and technicians of the University of Liverpool's Rock Deformation Laboratory (Gary Coughlan) and Scanning Electron Microscopy Shared Research Facility (Elliot Wood) for access to, use of, and training on equipment and microscopes.

Author contributions
AM planned study strategy, made the rock samples for the tests, designed the jig for Brazilian test, performed all scientific experiments and measurements, analysed and interpreted the experiments' data, observed thin sections at optical and SEM microscopes, built up graphs for the data interpretations, designed a schematic illustration of the sample assembly, made all the data tables presenting data collections, contributed in writing the manuscript. DRF planned study strategy, supervised laboratory operations, analysed and interpreted the experiments' data, contributed in writing the manuscript. DDM planned study strategy, provided rough rock samples from the field, collected SEM images, analysed and interpreted the experiments' data, contributed in writing the manuscript. All authors read and approved the final manuscript.

Funding
This research was supported and funded by the New Zealand Ministry of Business, Innovation and Employment Geothermal Supermodels research programme hosted by GNS Science.

Availability of data and materials
The datasets used and analysed during the current study are available and have been attached as submitting files. Information and settings about the machines employed in the experiments are available at Rock Deformation Laboratory—Department of Earth, Ocean and Ecological Sciences—University of Liverpool (UK).

Declarations

Competing interests
The authors declare that they have no competing interests regarding the publication of this article.

Received: 12 November 2021 Accepted: 9 May 2022
Published online: 28 June 2022

References

Adams CJ, Mortimer N, Campbell HJ, Griffin WL. Age and isotropic characterisation of metasedimentary rocks from the Torlesse Supergroup and Waipapa Group in the central North Island, New Zealand. NZ J Geol Geophys. 2009;52:149–70. https://doi.org/10.1080/00288300909509883.

Aliyu MD, Archer RA. Numerical simulation of multifracture HDR geothermal reservoirs. Renewable Energy. 2021;164:541–55. https://doi.org/10.1016/j.renene.2020.09.085.

ASTM, 2008, Standard Test Method for Splitting Tensile Strength of Intact Rock Core Specimens (D3967—08), American Society for Testing and Materials (ASTM), West Conshohocken, pp.1-3. https://doi.org/10.1520/D3967-08

Bayrante LF, Spörli KB. Structural observations in the autochthon and allochthon at Ngawha geothermal field, New Zealand. Geology of Northland: Accretion, allochthon and arcs at the edge of the New Zealand micro-continent. R Soc N Z Bull. 1989;26:106–14.

Beetham RD, Watters WA. Geology of Torlesse and Waipapa terrane basement rocks encountered during the Tongariro power development project, North Island, New Zealand. NZ J Geol Geophys. 1985;28:575–94. https://doi.org/10.1080/00288306.1985.10422534.

Begg JG, Mazengarb C. Part Q27, scale 1:50,000, Lower Hutt: Institute of Geological & Nuclear Sciences. Institute of Geological & Nuclear Sciences geological map 22. 128 p. + 1 fold. Map. 1996.
Bibby H, Caldwell T, Davey F, Webb T. Geophysical evidence on the structure of the Taupo Volcanic Zone and its hydrothermal circulation. J Volcanol Geoth Res. 1995;68:29–58. https://doi.org/10.1016/0377-0273(95)00007-H.
Bignall G. Taupo Volcanic Zone deep geothermal drilling project. Proceedings Hotter and Deeper Exploration Science Workshop, Taupo, New Zealand. 2011. https://www.geothermal-energy.org/pdf/IGAstandard/NZGW/2011/K2.pdf
Bignall G, Rae A, Rosenberg M. Rationale for targeting fault versus formation-hosted permeability in high-temperature geothermal systems of the Taupo Volcanic Zone, New Zealand. Proceedings, World Geothermal Congress, Bali, Indonesia. 2010. https://www.geothermal-energy.org/pdf/IGAstandard/WGC/2010/1148.pdf
Blake OO, Faulkner DR, Rietbrock A. The effect of varying damage history in crystalline rocks on the P and S wave velocity under hydrostatic confining pressure. Pure Applied Geophysics. 2012;170:493–505. https://doi.org/10.1617/s11527-016-0892-7.
Brace WF, Walsh JB, Frangos WT. Permeability of granite under high pressure. J Geophys Res. 1968;73:2225–36. https://doi.org/10.1029/JB073i006p02225.
Brathwaite RL, Wood CP, Rosenberg MD, Faure K. Porosity and permeability in the basement rocks at the Kawerau and Ohaaki geothermal fields, New Zealand. IN: Soengkono S, Browne PRL. Proceedings, 24th New Zealand Geothermal Workshop, University of Auckland. 2002;24:49–54. https://www.geothermal-energy.org/pdf/IGAstandard/NZGW/2002/Brathwaite.pdf. Accessed 31 October 2021.
Browne PRL. Joint channels in reservoir rocks of the Ngawha geothermal field, Northland. In: Proceeding, 2nd New Zealand Geothermal Workshop, University of Auckland. 1980;81–84. https://www.geothermal-energy.org/pdf/IGAstandard/NZGW/1980/Browne.pdf
Cant JL, Siratovich PA, Cole JW, Villeneuve MC, Kennedy BM. Matrix permeability of reservoir rocks, Ngatamariki geothermal field, Taupo Volcanic Zone, New Zealand. Geothermal Energy. 2018 https://doi.org/10.26021/8877
Carey B, Dunstall M, McClintock S, White B, Bignall G, Luketina K, Robson B, Zarrouk S, Seyward A. New Zealand country update. World Geothermal Congress, Melbourne. 2015.
Chaki S, Takarli M, Agbodjan WP. Influence of thermal damage on physical properties of a granite rock: porosity, permeability and ultrasonic wave evolutions. Construct Build Mater. 2008;22:1456–61. https://doi.org/10.1016/j.conbuildmat.2007.04.002.
Cole JW, Spinks KD. Caldera volcanism and rift structure in the Taupo Volcanic Zone, New Zealand. Geolo Soc. 2009;327:9–29. https://doi.org/10.1144/SP327.2.
Costa A. Permeability-porosity relationship: A reexamination of the Kozeny-Carman equation based on a fractal pore-space geometry assumption. Geophys Res Lett. 2006. https://doi.org/10.1029/2005GL025134.
Cox ME, Browne PRL. Hydrothermal alteration mineralogy as an indicator of hydrology at the Ngawha Geothermal Field. New Zealand Geothermics. 1998;27:259–70. https://doi.org/10.1016/S0375-6505(97)10015-3.
Davatzes NC, Hickman SH. The feedback between stress, faulting, and fluid flow: Lessons from the Coso Geothermal Field, CA, USA. In Proceedings World Geothermal Congress. 2010;1–14.https://www.geothermal-energy.org/pdf/IGAstandard/WGC/2010/1267.pdf.
De Paola N, Faulkner DR, Collettini C. Brittle versus ductile deformation as the main control on the transport properties of low-porosity anhydrite rocks. J Geophys Res. 2009;114:B06211. https://doi.org/10.1029/2008JB005967.
Di Pippo R. Geothermal power plants: principles, applications, case studies and environmental impact. 2nd ed. Oxford: Elsevier Ltd; 2008.
Eberhardt E, Stead D, Stimpson B. Quantifying progressive pre-peak brittle fracture damage in rock during uniaxial compression. Int J Rock Mech Min Sci. 1999;36:361–80. https://doi.org/10.1016/S0148-9062(99)00019-4.
Eggertsson GH, Lavallée Y, Kendrick JE, Markússon SH. Improving fluid flow in geothermal reservoirs by thermal and mechanical stimulation: The case of Krafla volcano, Iceland. J Volcanol Geoth Res. 2020;391: 106351. https://doi.org/10.1016/j.jvolgeores.2018.04.008.
Evans KF, Genter A, Sausse J. Permeability creation and damage due to massive fluid injections into granite at 35 km at Soultz: 1 Borehole observations. J Geophys Res Solid Earth. 2005;110:B4. https://doi.org/10.1029/2004JB003168.
Faulkner DR, Armitage PJ. The effect of tectonic environment on permeability development around faults and in the brittle crust. Earth Planet Sci Lett. 2013;375:71–7. https://doi.org/10.1016/j.epsl.2013.05.006.
Faulkner DR, Mitchell TM, Healy D, Heap MJ. Slip on "weak" faults by the rotation of regional stress in the fracture damage zone. Nature. 2006;444:922–5. https://doi.org/10.1038/nature05353.
Faulkner DR, Sanchez-Roa C, Boulton C, den Hartog, SAM. Pore fluid pressure development in compacting fault gouge in theory, experiments, and nature. J Geophys Res Solid Earth. 2018;123:226–41. https://doi.org/10.1002/2017JB015130.
Fortin J, Stanchits S, Vinciguerra S, Guéguen Y. Influence of thermal and mechanical cracks on permeability and elastic wave velocities in a basalt from Mt Etna volcano subjected to elevated pressure. Tectonophysics. 2011;503:60–74. https://doi.org/10.1016/J.TECTO.2010.09.028.
Gale JFW, Holder J. Natural fractures in the Barnett Shale: Constraints on spatial organization and tensile strength with implications for hydraulic fracture treatment in Shale-Gas reservoirs. In: 42nd U.S. Rock Mechanics Symposium & 2nd U.S.-Canada Rock Mechanics Symposium: ARMA. 2008;08–96.
Graf T, Therrien R. Stable–unstable flow of geothermal fluids in fractured rock. Geofluids. 2009;9:138–52. https://doi.org/10.1111/J.1468-8123.2008.00233.
Grant MA, Bixley PF. Geothermal Reservoir Engineering. 2nd ed. Burlington: Academic Press; 2011.
Gupta H, Sukanta R. An alternative resource for the 21st Century. Geothermal Energy, 1st edition, Elsevier Science. 2006.
Healy D, Jones RR, Holdsworth RE. Three-dimensional brittle shear fracturing by tensile crack interaction. Nature. 2006;439:64–7. https://doi.org/10.1038/nature04346.
Heap MJ, Faulkner DR. Quantifying the evolution of static elastic properties as crystalline rock approaches failure. Int J Rock Mech Min Sci. 2008;45:564–73.

Heap MJ, Gilg HA, Byrne PK, Wadsworth FB, Reuschlé T. Petrophysical properties, mechanical behaviour, and failure modes of impact melt-bearing breccia (suevite) from the Ries impact crater (Germany). Icarus. 2020a;349: 113873. https://doi.org/10.1016/j.icarus.2020.113873.
Heap MJ, Gravley DM, Kennedy BM, Gilg HA, Bertolett E, Barker SL. Quantifying the role of hydrothermal alteration in creating geothermal and epithermal mineral resources: the Ohakuri ignimbrite (Taupō Volcanic Zone, New Zealand). J Volcanol Geoth Res. 2020b;390: 106703. https://doi.org/10.1016/j.jvolgeores.2019.106703.
Heap MJ, Kennedy B. Exploring the scale-dependent permeability of fractured andesite. Earth Planet Sci Lett. 2016;447:139–50. https://doi.org/10.1016/j.epsl.2016.05.004.
Heap MJ, Lavallée Y, Petrakova L, Baud P, Reuschlé T, Varley NR, Dingwell DB. Microstructural controls on the physical and mechanical properties of edifice-forming andesites at Volcán de Colima, Mexico. J Geophys Res Solid Earth. 2014;119:2925–63. https://doi.org/10.1002/2013JB010521.
Kushnir AR, Heap MJ, Baud P. Assessing the role of fractures on the permeability of the Permo-Triassic sandstones at the Soultz-sous-Forêts (France) geothermal site. Geothermics. 2018;74:181–9. https://doi.org/10.1016/j.geothermics.2018.03.009.
Kuttruff H. Ultrasonics fundamentals and applications. Science & Technology, New York: Elsevier; 1991.
Lajtai EZ. Microscopic fracture processes in a granite. Rock Mech Rock Eng. 1998;31:237–50. https://doi.org/10.1007/s006030050023.
Lamur A, Kendrick JE, Eggertsson GH, Wall RJ, Ashworth JD, Lavallée Y. The permeability of fractured rocks in pressurised volcanic and geothermal systems. Sci Rep. 2017;7:61–73. https://doi.org/10.1038/s41598-017-05460-4.
Lockner DA, Byerlee JD, Kuksenko V, Ponomarev A, Sidorin A. Quasi-static fault growth and shear fracture energy in granite. Nature. 1991;350:39–42. https://doi.org/10.1038/350039a0.
Lockner DA, Byerlee JD, Kuksenko V, Ponomarev A, Sidrin A. Observations of quasi-static fault growth from acoustic emissions. In: Evans B, Wong TF, editors. Fault Mechanics and Transport Properties of Rocks. Academic, San Diego: California; 1992. p. 3–31.
Mayer W. Petrology of the Waipapa Group, near Auckland, New Zealand. NZ J Geol Geophys. 1968;12:412–35. https://doi.org/10.1080/00288306.1969.10420291.
McGuinness MJ. Recent interference tests at Ngawha and Ohaaki. Proceedings, 6th New Zealand Geothermal Workshop. 1984. p. 169–174. https://pangea.stanford.edu/ERE/pdf/IGAstandard/NZGW/1984/McGuinness.pdf.
McNamara DD, Faulkner DR, McCarney E. Rock Properties of Greywacke Basement Hosting Geothermal Reservoirs, New Zealand, preliminary results. Proceedings, 39th Workshop Geothermal Reservoir Engineering, Stanford University, California. 2014;10–21.
McNamara DD, Lister A, Prior DJ. Calcite sealing in a fractured geothermal reservoir: Insights from combined EBSD and chemistry mapping. J Volcanol Geoth Res. 2016a;323:38–52. https://doi.org/10.1016/j.jvolgeores.2016.04.042.
McNamara DD, Massiot C. Geothermal structural geology in New Zealand: Innovative Characterisation and micro-analytical techniques. Proceedings, 38th New Zealand Geothermal Workshop, Auckland, New Zealand. 2016. https://www.geothermal-energy.org/pdf/IGAstandard/NZGW/2016/Keynote_McNamara.pdf (2016). Accessed 31 October 2021.
McNamara DD, Milicich SD, Massiot C, Villamor P, McLean K, Sépulveda F, Ries WF. Tectonic controls on Taupo Volcanic Zone geothermal expression: Insights from Te Mihi. Wairakei Geothermal Field Tectonics. 2019. https://doi.org/10.1029/2018TC005296.
McNamara DD, Sewell S, Buscarlet E, Wallis IC. A review of the Rotokawa Geothermal Field. New Zealand Geothermics. 2016b;59:281–93. https://doi.org/10.1016/j.geothermics.2015.07.007.
Mielke P, Weinert S, Bignall G, Sass I. Thermo-physical rock properties of greywacke basement rock and intrusive lavas from the Taupo Volcanic Zone, New Zealand. J Volcanol Geoth Res. 2016;324:179–89. https://doi.org/10.1016/j.jvolgeores.2016.06.002.
Milicich SD, Clark JP, Wong C, Askari M. A review of the Kawerau geothermal field. New Zealand Geothermics. 2016;59:252–65. https://doi.org/10.1016/j.jvolgeores.2018.01.012.
Milicich SD, Wilson CJN, Bignall G, Pezaro B, Charlier BLA, Wooden JL, Ireland TR. U-Pb dating of zircon in hydrothermally altered rocks of the Kawerau Geothermal Field, Taupo Volcanic Zone, New Zealand. J Volcanol Geoth Res. 2013;253:97–113. https://doi.org/10.1016/j.jvolgeores.2012.12.016.
Mitchell TM, Faulkner DR. Experimental measurements of permeability evolution during triaxial compression of initially intact crystalline rocks and implications for fluid flow in fault zones. 2008. J Geophys Res. https://doi.org/10.1029/2008JB005588.
Mongillo MA. The Ngawha geothermal field: new and updated scientific investigations. Geothermal Coordination Group, Department of Scientific and Industrial Research. 1985.
Mroczek EK, Milicich SD, Bixley PF, Sepulveda F, Bertrand EA, Soengkono S, Rae AJ. Ohaaki geothermal system: Refinement of a conceptual reservoir model. Geothermics. 2016;59:311–24. https://doi.org/10.1016/j.geothermics.2015.09.002.
Nara Y, Meredith PG, Yoneda T, Kaneko K. Influence of macro-fractures and micro-fractures on permeability and elastic wave velocities in basalt at elevated pressure. Tectonophysics. 2011;503:52–9. https://doi.org/10.1016/j.tecto.2010.09.027.
O'Connell RJ, Budiansky B. Seismic velocities in dry and saturated cracked solids. J Geophys Res. 1974;79:5412–26. https://doi.org/10.1029/JB079i035p05412.
Passelègue FX, Pimienta L, Faulkner DR, Schubnel A, Fortin JN, Guéguen Y. Development and recovery of stress-induced elastic anisotropy during cyclic loading experiment on Westerley granite. Geophys Res Lett. 2018;45:8156–816.
Paterson M, Wong T. Experimental rock deformation—the brittle field. Berlin: Springer; 2005. p. 12–3.
Pérez-Flores P, Wang G, Mitchell TM, Meredith PG, Nara Y, Sarkar V, Cembrano J. The effect of offset on fracture permeability of rocks from the Southern Andes Volcanic Zone. Chile J Struct Geol. 2017;104:142–58. https://doi.org/10.1016/j.jsg.2017.09.015.
Reches Z, Lockner DA. Nucleation and growth of faults in brittle rocks. J Geophys Res. 1994;99:159–73. https://doi.org/10.1029/94JB00115.

Richards L, Read S. New Zealand greywacke characteristics and influences on rock mass behavior. In: Proceedings, 11th Congress of the International Society of Rock Mechanics: the second half century of rock mechanics. 2007. p. 359–364.
Rowland JV, Sibson RH. Structural controls on hydrothermal flow in a segmented rift system, Taupo Volcanic Zone. New Zealand Geofluids. 2004;4:259–83. https://doi.org/10.1111/j.1468-8123.2004.00091.x.
Rutter EH, Mecklenburgh J. Influence of normal and shear stress on the hydraulic transmissivity of thin cracks in a tight quartz sandstone, a granite, and a shale. Geophys Res Solid Earth. 2018. https://doi.org/10.1002/2017JB014858.
Schubnel A, Nishizawa O, Masuda K, Lei XJ, Xue Z, Guéguen Y. Velocity measurements and crack density determination during wet triaxial experiments on Oshima and Toki granites. Pure Appl Geophys 2003;160:869–87. https://doi.org/10.1007/PL00012570.
Sheppard DS. Fluid chemistry of the Waimangu geothermal system. Geothermics. 1986;15:309–28. https://doi.org/10.1016/0375-6505(86)90107-0.
Sherburn S, Bannister SC, Bibby HM. Seismic velocity structure of the central Taupo Volcanic Zone, New Zealand, from local earthquake tomography. J Volcanol Geoth Res. 2003;122:69–88. https://doi.org/10.1016/S0377-0273(02)00470-5.
Siratovich PA, Davidson J, Villeneuve M, Graveley D, Kennedy B, Cole J, Wyering L, Price L. Physical and mechanical properties of the Rotokawa Andesite from production wells RK 27_L2, RK 28 and RK 30. Proceedings, New Zealand Geothermal Workshop, University of Auckland, New Zealand. 2012. https://www.geothermal-energy.org/pdf/IGAstandard/NZGW/2012/46654final00022.pdf
Siratovich PA, Heap MJ, Villeneuve MC, Cole JW, Reuschlé T. Physical property relationships of the Rotokawa Andesite, a significant geothermal reservoir rock in the Taupo Volcanic Zone. New Zealand Geothermal Energy. 2014;2:1–31. https://doi.org/10.1186/s40517-014-0010-4.
Siratovich PA, Von Aulock FW, Lavallée Y, Cole JW, Kennedy BM, Villeneuve MC. Thermoelastic properties of the Rotokawa Andesite: A geothermal reservoir constraint. J Volcanol Geoth Res. 2015;301:1–13. https://doi.org/10.1016/j.jvolgeores.2015.05.003.
Stewart S. Rock mass strength and deformability of unweathered closely jointed New Zealand greywacke, PhD Thesis, University of Canterbury, Christchurch, New Zealand. 2007. http://dx.doi.org/https://doi.org/10.26021/3499
Sutherland R, Townend J, Toy V, Zimmer M. Extreme hydrothermal conditions at an active plate-bounding fault. Nature. 2017;546:137–40. https://doi.org/10.1038/nature22355.
Vinciguerra S, Trovato C, Meredith PG, Benson PM. Relating seismic velocities, thermal cracking and permeability in Mt Etna and Iceland basalts. Int J Rock Mech Mining Sci. 2005;42:900–10. https://doi.org/10.1016/j.ijrmms.2005.05.022.
Wallis I, McNamara DD, Rowland J, Massiot C. The nature of fracture permeability in the greywacke basement at Kawerau Geothermal Field, New Zealand. In: Proceedings, 37th Workshop on Geothermal Reservoir Engineering. 2012. https://doi.org/10.13140/RG.2.1.4875.9284
Wallis IC, Bardsley CJ, Powell TS, Rowland JV, O'Brien JM. A structural model for the Rotokawa Geothermal Field, New Zealand. In: Proceedings, 35th New Zealand Geothermal Workshop, Auckland University, New Zealand. 2013.
Wang G, Mitchell TM, Meredith PG, Nara Y, Wu Z. Influence of gouge thickness and grain size on permeability of macrofractured basalt. J Geophys Res Solid Earth. 2016;121:8472–87. https://doi.org/10.1002/2016JB013363.
Wilson CJN, Houghton BF, McWilliams MO, Lanphere MA, Weaver SD, Briggs RM. Volcanic and structural evolution of Taupo Volcanic Zone, New Zealand, a review. J Volcanol Geoth Res. 1995;68:1–28.
Wood C, Brathwaite RL, Rosenberg MD. Basement structure, lithology and permeability at Kawerau and Ohaaki geothermal fields. New Zealand Geothermics. 2001;30:461–81. https://doi.org/10.1016/S0375-6505(01)00003-7.
Wyering LD, Villeneuve MC, Walli IC, Siratovich PA, Kennedy BM, Gravley DM, Cant JL. Mechanical and physical properties of hydrothermally altered rocks, Taupo Volcanic Zone. New Zealand. 2014. https://doi.org/10.1016/j.jvolgeores.2014.10.008.
Zoback MD, Byerlee JD. The effect of microcrack dilatancy on the permeability of Westerly granite. J Geophys Res. 1975;80:752–5. https://doi.org/10.1029/JB080i005p00752.

Publisher's Note